

# On the Origin of Wind Line Variability in O Stars

D. Massa

*Space Science Institute, 4750 Walnut Street, Suite 205, Boulder, CO 80301*

`dmassa@spacescience.org`

and

R. K. Prinja

*Department of Physics and Astronomy, University College London, Gower Street, London WC1E 6BT*

## ABSTRACT

We analyze 10 UV time series for 5 stars which fulfill specific sampling and spectral criteria to constrain the origin of large-scale wind structure in O stars. We argue that excited state lines must arise close to the stellar surface and are an excellent diagnostic complement to resonance lines which, due to radiative transfer effects, rarely show variability at low velocity. Consequently, we splice dynamic spectra of the excited state line, N IV  $\lambda 1718$ , at low velocity to those of Si IV  $\lambda \lambda 1400$  at high velocity in order to examine the temporal evolution of wind line features. These spliced time series reveal that nearly all of the features observed in the time series originate at or very near the stellar surface. Further, we positively identify the observational signature of equatorial co-rotating interaction regions in two of the five stars and possibly two others. In addition, we see no evidence for features originating further out in the wind. We use our results to consolidate the fact that the features seen in dynamic spectra must be huge, in order to remain in the line of sight for days, persisting to very large velocity and that the photospheric footprint of the features must also be quite large,  $\sim 15 - 20\%$  of the stellar diameter.

*Subject headings:* stars: winds, outflows, stars: massive, stars: mass-loss, stars: activity

## 1. Introduction

Revealing the systematic spectral variability of OB star wind lines was a major contribution of the *International Ultraviolet Explorer (IUE)* (e.g., Massa et al. 1995, Kaper et al. 1996, k96

hereafter). These observations demonstrated that the source of the variability was large, coherent structures in the winds (e.g., Fullerton et al. 1997, Kaper et al. (1999, k99 hereafter), de Jong et al. 2001, Prinja et al. 2002). Since then, similar evidence for large scale structure has been detected in the winds of LMC O stars (Massa et al. 2000), the central stars of planetary nebulae (Prinja, Massa & Cantiello 2012), and may be a fundamental property of radiatively driven wind flows.

While the absorption features observed in time series propagate monotonically to higher velocity, they move more slowly than the velocity law of the wind (determined from the shapes of saturated wind lines) would predict. In fact, one often observes different features propagating with different accelerations at the same time. To explain this, Mullan (1984) proposed that the absorption features were the signatures of co-rotating interaction regions, CIRs, in the winds. These are similar to structures seen in the Solar wind, where different sectors of the stellar surface give rise to winds which accelerate differently. Rotation causes these different sectorial flows to interact, and an interface with a spiral pattern can result and a velocity plateau can develop along the interface. Then, as the CIR moves across our line of sight to the stellar disk, it can give the appearance of an absorption feature moving slowly outward in the wind. This explanation has considerable appeal, since it explains the slow acceleration of the absorption features, and the large spatially coherent structures can explain the persistence of the absorption features along the line of sight, which can persist for several days.

Cranmer & Owocki (1996) and Lobel & Blomme (2008) analyzed the time dependent signature of CIRs originating in the equatorial plane of a star when viewed equator-on. They showed that a specific wavelength dependent form of variability resulted, and they termed its shape “bananas”. This signature has been identified in the Si iv  $\lambda\lambda 1400$  wind lines of the B supergiants HD 64760 (Fullerton et al. 1997) and HD 150168 (Prinja et al. 2002), and the O star  $\xi$  Per (de Jong et al. 2001). In these cases, a photospheric origin for the variability seems secure. In fact, Ramiamananantsoa et al. (2014) detected optical photometric variability in  $\xi$  Per with a time scale similar to the DACs measured by de Jong et al., strengthening the case for a photospheric connection. In other cases, it is not clear whether the absorption features which appear at low velocity and propagate to high velocity actually originate near the stellar surface, or if they are the result of a density enhancement caused by low velocity material behind a shock further out in the wind, which then simply appears at low velocity.

The presence of structure can significantly affect the mass loss rate inferred from different spectral diagnostics and has been the focus of some recent observational (e.g., Fullerton et al. 2006, Prinja & Massa 2010, Prinja & Massa 2013) and theoretical (e.g., Sundqvist et al. 2010, S rlan et al. 2012) studies. The result has been a mass loss rate discrepancy, which refers to the large, up to a factor of 10, differences between the theoretical expectations (e.g., Muijres et al. 2012) and observationally determined mass loss rates derived from homogeneous wind models. Recent theoretical models have resolved much of this discrepancy by introducing optically thick structures in the wind. However, current models are based on winds containing randomly distributed, small scale blobs, and the results could be very different for large structures, such as CIRs. The reason

is that *geometry matters* for wind line formation in a wind containing large scale optically thick structures.

Determining whether the variability seen in the time series is due to material originating near or at the surface of the star and then propagating outward, or low speed material at large distances from the star which simply appears at low velocity is the goal of this paper. Should the origin of all of the features be tied to the stellar surface, this would have implications about the structure of the winds (how does the component of the wind which shapes saturated wind lines co-exist with large scale structure), the structure of the photosphere (what causes the photospheric irregularities that give rise to the different wind flows), X-ray production (do X-rays originate mainly in small, spatially incoherent shocks or along the interfaces of the CIRs) and the theoretical derivations and simulations based on a smooth wind.

In the following sections we: 1) provide a brief review of wind line formation and variability, emphasizing how excited state lines can be used to trace structures to the lower wind and to make a photospheric connection; 2) examine the available data sets for O stars with a well developed excited state line and arrive at our sample of time series; 3) demonstrate one new instance of a CIR in a time series for 68 Cyg, and possible CIR signatures in time series for  $\zeta$  Pup and  $\lambda$  Cep, and; 4) discuss the implications of our results.

## 2. Wind Line Formation

When discussing wind line variability, we confine ourselves to the UV lines and concentrate on the wind absorption. Variable emission in UV wind lines is rarely observed in OB stars, primarily because the emission at a given velocity is composed of light scattered throughout the wind, averaging over any inhomogeneities that may be present. In contrast, the absorption arises in the cylinder of wind material that lies between the stellar disk and the observer. The observed absorption is a function of wavelength or, equivalently, velocity.

Generally, there is no way to directly determine the radial location of an absorption feature at a specific velocity. For example, a low velocity feature could arise from material near the stellar surface, accelerating outward, or from slowly moving wind material far out in the wind, which is re-accelerating after being shocked. This ambiguity is always the case for resonance lines, but not for excited state lines. To see why this is so, we now provide a brief description of how the two different lines are formed.

A resonance wind line is effectively a pure scattering line. Anywhere an ion exists in the ground state, the resonance line will scatter incoming radiation. For a typical wind acceleration law, a resonance line will first become optically thick at low velocity, where the wind density is highest. As a result, wind lines that are strong enough to show variability at intermediate and high velocity are usually optically very thick at low velocity. Consequently, large changes in column density translate into small changes in the absorption. Two other factors also conspire to make the

variability of resonance lines difficult to observe at low velocity. The first is that the photospheric resonance line is typically very strong, so any line of sight absorption is seen against a very weak continuum. The second is that the scattered radiation originating from all over the wind peaks at low velocity. This means that any weak variation in the small residual flux at low velocity is masked by strong emission.

An excited state wind line arises from an allowed transition whose lower level is the upper level of a resonance transition (typically below  $900\text{\AA}$ ). They frequently appear as wind lines in O stars with strong mass fluxes. One of the most commonly observed excited state lines is N IV  $\lambda 1718$ , whose lower level is the upper level of the N IV  $\lambda 765$  resonance line. In most cases, a very simplified level population model can be used to accurately describe the population of the lower state of an excited state wind lines (e.g., Olson, 1981). H  $\alpha$  (and to a lesser degree He II  $\lambda 1640$ ) is a notable exception. Because H I is a trace ion in O star winds and lies on the only path to the ground state, its level populations are dominated by recombinations. An excited state line like N IV  $\lambda 1718$  has three important properties that make it a valuable diagnostic for variability studies. First, because a strong EUV radiation field is required to populate its lower level, it can only exist close to the star (this gives excited state lines their distinctive profiles). As a result, *a feature which appears at low velocity in N IV  $\lambda 1718$  must originate close to the stellar surface*, i.e., it cannot be a low velocity, post-shock region far out in the wind. Second, the photospheric N IV  $\lambda 1718$  line tends to be considerably weaker than a resonance line, so a variable absorption is viewed against a stronger continuum than for a resonance line. Third, because excited state lines become optically thin far from the star, the scattered light contribution at low velocity is much weaker. These properties make variability much easier to detect at low velocity in an excited state line. However, because excited state lines weaken quickly at large distances from the star, high velocity variability is difficult to detect.

We see, therefore, how resonance and excited state lines complement one another. If a feature (indicated by excess or reduced absorption) appears at low velocity in an excited state line and then joins a high velocity feature in a resonance line (whose low velocity portion may be saturated) at higher velocity, this provides evidence that the excess or deficiency of opacity which caused the feature close to the stellar surface (where the radiation field is intense) propagated outward, into the wind.

### 3. The Data

The *IUE* data base is the only one available containing the UV time series needed for analysis. To avoid radiative transfer effects, one would prefer to compare a resonance singlet and an excited state singlet. While N IV  $\lambda 1718$  is an ideal example of the latter, O star spectra do not have a suitable resonance singlet in the *IUE* wavelength band. Consequently, we were forced to use a doublet. In this case, Si IV  $\lambda\lambda 1400$  is the best candidate, since its doublet separation is large,  $\delta v = 1936 \text{ km s}^{-1}$ , and it is often strong but unsaturated in stars with well developed N IV  $\lambda 1718$ .

We concentrate on the blue component of the doublet because it is unaffected by the red component over the velocity range  $-v_\infty \leq v \leq -v_\infty + \delta v$  (Olson 1982). Thus, much of the high velocity portion of the blue component behaves as if it were a singlet. For example, the blue component of the Si IV doublet in a star with  $v_\infty = 2700 \text{ km s}^{-1}$  is unaffected by the red component over the velocity range  $-2700 \leq v \leq -764 \text{ km s}^{-1}$ . Figure 1 shows these intervals for  $\zeta$  Pup.

To arrive at our sample, we began with all the SWP high resolution observations of stars in *IUE* object classes 12–15, which stand for: main sequence O; supergiant O; Oe, and; Of. This consisted of 3401 spectra of 325 stars. The sample was then narrowed to stars with 10 or more spectra (54 stars) with sequential observations separated by less than 1 day (27 stars). We then imposed the following two constraints. First, the spectra must have distinctly asymmetric N IV  $\lambda 1718$  profiles, so that wind variability can be observed. Second, the series must cover 4 or more days to span enough time to determine whether features observed at low velocity in N IV appear later at high velocity in Si IV. The net result of this search was 12 potentially suitable time series of 6 stars.

Table 1 gives some basic properties of the stellar sample. The columns give: 1 – The star name, 2 – spectral types from Maíz-Apellániz et al. (2003), 3 – wind terminal velocities from Prinja et al. (1998) for HD 93843 and the compilation of Fullerton et al. (2006) for the rest, 4 – projected rotational velocities from Penny (1996), 5 – stellar radii (again from Fullerton et al. or Prinja et al.), and 6 – the number of time series inspected.

Table 2 summarizes the properties of the time series we will examine. The columns list: 1 – the star name, 2 – the duration of the series in days, 3 – the range of *IUE* high resolution image numbers which encompass the series, 4 – the number of spectra in the series, 5 – the dates spanned by the series, and 6 – comments on the individual series.

Unfortunately, a few of the time series are not very useful for our purposes. For example, the series for HD 93843 is a long, but very sparsely sampled series (see Prinja et al. 1998), with a mean sampling interval of 10.2 hr. Such sparse sampling makes it difficult to identify features at low velocity, where they are accelerating quickly. To quantify this, consider the time it takes a parcel of wind to accelerate from its initial velocity,  $v_1$ , to a specific velocity,  $v_2$ . We adopt a standard  $\beta$  law of the wind acceleration, which has the form,  $w = (1 - a/x)^\beta$ , where  $w = v/v_\infty$ ,  $x = r/R_\star$ , and  $a = 1 - w(x = 1)$ . Adopting  $\beta = 1$  (a common value for O stars), we find that the time it takes a parcel of wind material to accelerate from  $w_1$  to  $w_2$  is:

$$t_2 - t_1 = 193.3 \frac{aR_\star}{v_\infty} \left[ \frac{w_2 - w_1}{(1 - w_1)(1 - w_2)} + \ln \frac{w_2(1 - w_1)}{w_1(1 - w_2)} \right] \text{ hrs} \quad (1)$$

Equation (1) shows that it takes wind material  $\sim 4.9$  hours to accelerate from  $w = 0.02$  to  $w = 0.5$  (where features tend to be lost in N IV). While absorption features typically accelerate more slowly than this, the sampling is so sparse that it can easily miss the entire time evolution of low velocity N IV features. As a result, we eliminate the HD 93843 series from the following analysis. For similar reasons, we also drop the third series for  $\lambda$  Cep.

#### 4. Analysis

Our analysis is relatively simple, and based primarily on visual inspection of dynamic spectra. Dynamic spectra are images of time ordered spectra normalized by the mean spectrum of the series, i.e.,  $n_\lambda = f_\lambda / \langle f_\lambda \rangle$ . Figures 2 – 11 show dynamic spectra for the program stars. Each figure contains three dynamic spectra with time increasing upward (labeled by the number of days since the beginning of the series) plotted against normalized velocity,  $w = v/v_\infty$ , where the  $v_\infty$  values are taken from Table 1. Nearest neighbor interpolation was used to place the spectra on a linear time grid, and gaps appear whenever more than 5 hours elapsed between exposures. The vertical lines represent the rest wavelengths of the lines, the bar at the side of each set shows the color scale used, and the mean spectrum for the series is shown at the bottom of each panel. The first two panels of each figure are for the Si IV  $\lambda\lambda 1400$  resonance doublet and the N IV  $\lambda 1718$  excited state line and the minimum and maximum scaling for these are 1/1.4 to 1.4 and 1/1.2 to 1.2 respectively. The third panel shows the low speed portion of the N IV dynamic spectrum ( $v \leq 1000 \text{ km s}^{-1}$ ) spliced onto the high speed portion ( $v > 1000 \text{ km s}^{-1}$ ) of the Si IV one (Figure 1 shows the regions spliced from each line). We choose  $1000 \text{ km s}^{-1}$  so that the high speed portion of the blue component of the resonance doublet will be radiatively decoupled from the red component. Because the amplitude of the N IV variability near  $1000 \text{ km s}^{-1}$  is typically smaller than the that of Si IV, we rescale the N IV portion of the profile to make the amplitudes match. This was done as follows:

$$n'_\lambda = (n_\lambda - 1) \times Const + 1 \quad (2)$$

where a value of  $Const = 2.5$  was used for all of the time series except for  $\zeta$  Pup, which has very strong N IV, so a value of 1.5 was used. The minimum and maximum extents of the color range for the spliced profiles are 1/1.2 to 1.2.

Our final sample is biased toward rapidly rotating stars. This is a consequence of the findings by Prinja (1988), which determined that wind activity evolves more quickly in rapidly rotating stars, so later time series observations concentrated on these objects to maximize the activity that could be captured in a fixed amount of *IUE* observing time.

The remainder of this section summaries the result of each spliced time series.

**$\xi$  Per** (Figures 2 and 3): The first series for this star has been examined previously by k96, Kaper et al. (1997, k97 hereafter), and k99. The series lasts only 4.4 days. Nevertheless, during that time 2 major absorption events occur, and both of them appear to have the “banana” shape that is indicative of an equatorial CIR moving into the line of sight.

The second series was analyzed extensively by de Jong et al. (2001). It is roughly twice as long as the first and, as de Jong et al. point out, contains the signatures of at least 4 CIR passages.

**HD 34656** (Figure 4): Our time series for this star was previously analyzed by k96, k97, and k99. The dynamic spectrum contains four major absorption features Si IV, and all of these connect to low velocity features in N IV. While these features lack the signature of an equatorial CIR viewed

edge on, at least two of them appear to extend to  $v \simeq 0$ . Although faint, it seems clear that one can trace absorption features from  $(w, t) = (0.0, 1.3) \rightarrow (-0.7, 2.4)$ , and  $(0.0, 2.5) \rightarrow (-0.6, 3.1)$ .

**$\zeta$  Pup** (Figures 5 and 6): The first series for this star was analyzed by Prinja et al. (1992). It is poorly sampled for our purposes, with large gaps in the time coverage. Nevertheless, at least 3 features can be seen moving through the Si IV profile, and all of them appear to connect to low velocity features in N IV which extend to  $v \simeq 0$ .

The second series was described by Howarth et al. (1995). It is long and well sampled. Numerous features are apparent both Si IV and N IV, and all of them appear to join seamlessly, indicating that they all originate near or at the stellar surface. A few of the features (e.g., the ones near day 4, day 9 and day 14) may have CIR signatures.

**68 Cyg** (Figures 7 – 9): This star has the weakest N IV  $\lambda 1718$  of the sample. The first series has been discussed several times in the past (Prinja 1988, Prinja & Howarth, 1988, k96, k97, k99). This series is poorly sampled for our purposes. Nevertheless, there are good indications that the high and low velocity features join. Specifically, the feature between days 5 and 6 and the two between days 3 and 5 appear to connect. The large gaps in coverage for the rest of the series makes it impossible to draw conclusions about the remainder of the features seen in Si IV.

The second 68 Cyg series was analyzed by Howarth & Smith (1995), k96, k97 and k99. It is a short, but well sampled series and it is quite clear that all of the high velocity features seen in Si IV join low velocity features in N IV.

The third 68 Cyg series has not been presented previously. It is fairly well sampled and considerably longer than the others. Once again, in spite of the weakness of the N IV variability, it is apparent that all of the high and low velocity features join. In fact, an equatorial CIR signature is apparent in many of them.

**$\lambda$  Cep** (Figures 10 and 11): The first series for this was included in k96, k97, and k99. It is poorly sampled with large gaps in the coverage. In spite of the poor coverage, it is possible to follow some of the features to zero velocity, and those that cannot be followed are due to poor coverage.

The second  $\lambda$  Cep series was also included in k96, k97 and k99. It is well sampled and presents an excellent example of distinct high and low velocity features joining seamlessly. The feature that straddles day 1 hints of having a CIR signature.

## 5. Discussion

We begin by summarizing our main observational results. We then discuss their implications for the structure of O star winds. Finally, we highlight some issues that must be resolved before we can arrive at a complete understanding of OB star winds.

Our main observational results are the following:

1. Every absorption feature observed at low velocity connects to a feature at high velocity.
2. Conversely, whenever the data allow it, every feature observed at high velocity can be traced to a feature at low velocity.
3. Some of the spliced Si IV– N IV dynamic spectra reveal “bananas”, which are the accepted signatures of CIRs tied to the stellar surface.
4. We see evidence of an equatorial CIR in 68 Cyg for the first time, and possible equatorial CIR signatures in spliced time series for  $\zeta$  Pup and  $\lambda$  Cep.
5. Since our technique reveals CIR signatures which almost certainly indicate the presence of spiral arms in the winds, we suspect that the other features which extend to  $v \simeq 0$  are also caused by CIRs, just not in the equatorial plane, or viewed edge on.

These results have the following implications on the structure of OB star winds:

1. The fact that features observed at low velocity in excited state lines join seamlessly to features at high velocity lines and vice versa, establishes a connection between the wind features and the stellar surface.
2. For the series analyzed, we see no evidence for features formed at intermediate velocity in the wind, i.e., all features can be traced back to the surface and they move through the profile monotonically with velocity. This implies the features are not formed by shocked gas far from the star, but by some mechanism very close to or on the stellar surface.
3. As has been known for a long time, the features seen in dynamic spectra must be huge, in order to remain in the line of sight for days, persisting to very large velocity.
4. For a feature to be detected at  $v \simeq 0$ , it must cause a 2 – 4% (Howarth & Smith, 1995) decrease in the flux or, equivalently, occult at least 2 – 4% of the stellar disk. This means that the linear size of the region responsible for the excess absorption must be  $\sim 15$  to 20% of the stellar diameter and, in some cases, considerably larger.

While the current results represent real progress, several open questions remain and we now describe a few of them. First, the stars in our sample which have been monitored at optical wavelengths show only very small amplitude photometric variability (Howarth & Stevens 2014, Ramaramananantsoa et al., 2014). Because we have shown that the photospheric footprints of the variability must be quite large, this implies that either the temperature difference between the footprints and the surrounding regions is very small or else the wind structures arise from small, randomly distributed irregularities which somehow organize themselves into large scale wind structures very near the stellar surface. Second, it is currently thought that the X-rays originate from small, spatially incoherent shocks distributed throughout the wind (e.g., Cohen et al. 2014).



However, when monitored in X-rays,  $\zeta$  Pup (Nazé et al. 2013) showed no evidence for variability on short time scales, implying that if the X-rays are produced by small scale structures, there must be thousands of them present at any given time. On the other hand, both  $\zeta$  Pup and  $\xi$  Per (Massa et al. 2014) exhibit X-ray variability on time scales that are more consistent with the those of the large structures we observe in the UV wind lines. Three possible explanations are: 1) the CIRs shepherd the clumps (although exactly how this occurs is not clear); 2) the CIRs occult some of the clumps as they sweep across the line of sight (but this requires them to be optically thick to X-rays and carry considerably more mass than currently believed), or; 3) the CIRs themselves are the source of the X-rays and, since they are large, coherent structures, short time scale variability is not expected (such a model has not been examined). Whatever the case, the fact that X-rays vary on a time scale consistent with the spiral structures observed in the UV wind lines highlights a short coming of our current understanding how OB star winds are structured. Third, we know that the UV spectral diagnostics used to derive mass loss rates in OB stars are strongly affected by optically thick structures (Massa et al. 2008, Prinja & Massa 2010). Further, Sundqvist et al. (2010) and Sürhan et al. (2013) have demonstrated how small, optically thick clumps can affect the diagnostics. However, for large scale, optically thick structures, geometry matters, i.e., the exact location and velocity of the structures affects the resulting wind line profiles, but to what extent is not at all clear. While CIRs may have a small effect on the mass loss rates (Lobel & Blomme 2008), they can have a profound effect on the wind lines. This is because they are thought to form in a velocity plateau, which can make their optical depths as much as 100 times larger than the ambient wind (see, Cranmer & Owocki 1996). Further, CIRs can affect a large velocity range at any given time (see, Figure 3 in Owocki et al. 1995). Unlike the small scale structures, the effects that optically thick CIRs may have on wind lines have not been modeled. Consequently, it is not clear how much of an effect they can have on our interpretations of observed profiles. Finally, we note that according to Cranmer & Owocki (1996), the DACs are caused by a non-monotonic velocity law. This occurs when the faster wind collides with the slower wind. For this mechanism to be responsible for what we observe, the two winds must interact very close to the stellar surface. While this is not typical for CIR formation, it is not impossible, and sets a strong constraint on the winds from the two regions that create the CIRs.

We thank Alex Fullerton for useful discussions and the referee for helpful comments on how to clarify and focus the presentation. DM acknowledges support from NASA’s Astrophysics Data Analysis Program through Grant NNX14AB30G. The data presented in this paper were obtained from the Mikulski Archive for Space Telescopes (MAST). STScI is operated by the Association of Universities for Research in Astronomy, Inc., under NASA contract NAS5-26555. Support for MAST for non-HST data is provided by the NASA Office of Space Science via grant NNX13AC07G and by other grants and contracts.

## REFERENCES

- Cohen, D.H., Wollman, E.E., Leutenegger, M.A., Sundqvist, J.O., Fullerton, A.W., Zsargó, J. & Owocki, S.P. 2014, MNRAS, 439, 908
- Cranmer, S.R. & Owocki, S.P. 1996, ApJ, 462, 469
- de Jong, J. A., Henrichs, H.F., Kaper, L., Nichols, J.S., Bjorkman, K., Bohlender, D.A., Cao, H., Gordon, K., Hill, G., Jiang, Y., Kolka, I., Morrison, N., Neff, J., O’Neal, D., Scheers, B. & Telting, J.H. 2001, A&A, 368, 601
- Fullerton, A.W., Massa, D.L., Prinja, R.K., Owocki, S.P. & Cranmer, S.R. 1997, A&A, 327, 699
- Fullerton, A.W., Massa, D.L. & Prinja, R.K. 2006, ApJ, 637, 1025
- Howarth, I.D., Prinja, R.K., Massa, D. 1995, ApJ, 452L, 65
- Howarth, I.D. & Smith, K.C. 1995, ApJ, 439, 431
- Howarth, Ian D. & Stevens, I-R. 2014, MNRAS, 445, 2878
- Howarth, I.D. & Smith, K.C. 1995, ApJ, 439, 431
- Kaper, L., Henrichs, H.F., Nichols, J.S., Snoek, L.C., Volten, H. & Zwarthoed, G.A.A. 1996 A&AS, 116, 257 (k96)
- Kaper, L., Henrichs, H.F., Fullerton, A.W., Ando, H., Bjorkman, K.S., Gies, D.R., Hirata, R., Kambe, E., McDavid, D. & Nichols, J.S. 1997, A&A, 327, 281 (k97)
- Kaper, L., Henrichs, H.F., Nichols, J.S. & Telting, J.H. 1999, A&A, 344, 231 (k99)
- Lobel, A. & Blomme, R. 2008, ApJ, 678, 408
- Maíz-Apellániz, J., Walborn, N.R., Galué, H.A., & Wei, L.H. 2004, ApJS, 151, 103.
- Massa, D., Fullerton, A.W., Nichols, J.S., Owocki, S.P., Prinja, R.K., St-Louis, N., Willis, A.J., Altner, B., Bolton, C.T., Cassinelli, J.P. et al. 1995, ApJ, 452L, 53
- Massa, D., Fullerton, A.W., Hutchings, J.B., Morton, D.C., Sonneborn, G., Willis, A.J., Bianchi, L., Brownsberger, K.R., Crowther, P.A., Snow, T.P. & York, D.G. 2000 ApJ, 538L, 47
- Massa, D.L., Prinja, R.K., & Fullerton, A.W. 2008, in Clumping in Hot-Star Winds, ed. W.-R. Hamann, A. Feldmeier, & L. M. Oskinova, 147
- Massa, D., Oskinova, L., Fullerton, A.W., Prinja, R.K., Bohlender, D.A., Morrison, N.D., Blake, M. & Pych, W. 2014, MNRAS, 441, 2173
- Muijres, L.E., Vink, J.S., de Koter, A., Müller, P.E. & Langer, N. 2012, A&A, 537A, 37

- Mullan, D.J. 1984, ApJ, 283, 303
- Nazé, Y., Oskinova, L. M. & Gosset, E. 2013, ApJ, 763, 143
- Olson, G.L. 1982, ApJ, 255, 267
- Olson, G.L. 1981, ApJ, 245, 1054
- Owocki, S.P., Cramner, S.R. & Fullert, A.W 1995, ApJ, 453, L37
- Penny, L.F. 1996, ApJ, 463, 737
- Prinja, R.K. 1988, MNRAS, 231P, 21
- Prinja, R. K., Balona, L.A., Bolton, C.T., Crowe, R.A., Fieldus, M.S., Fullerton, A.W., Gies, D.R., Howarth, I.D., McDavid, D. & Reid, A.H.N. 1992, ApJ, 390, 266
- Prinja, R.K., Howarth, I.D. 1988, MNRAS, 233, 123
- Prinja, R.K., Massa, D., Howarth, I.D. & Fullerton, A.W. 1998, MNRAS, 301, 926
- Prinja, R.K., Massa, D. & Fullerton, A.W. 2002, A&A, 388, 587
- Prinja, R.K. & Massa 2010, A&A, 521L, 55
- Prinja, R.K. & Massa 2013, A&A, 559A, 15
- Prinja, R.K., Massa, D.L. & Cantiello, M. 2012, ApJ, 759L, 28
- Ramiamananantsoa, T., Moffat, A.F.J., Chené, A-N, Richardson, N.D., Henrichs, H.F., Desforges, S., Antoci, V., Rowe, J.F., Matthews, J.M., Kuschnig, R., et al. 2014, MNRAS, 441, 910
- Sundqvist, J.O., Puls, J. & Feldmeier, A. 2010, A&A, 510A, 11
- Sürlan, B., Hamann, W.-R., Aret, A., Kubát, J., Oskinova, L.M. & Torres, A.F. 2013, A&A, 559A, 130

Table 1: Program Stars

Name	Sp Ty	$v_{\infty}$ km s <sup>-1</sup>	$v \sin i$ km s <sup>-1</sup>	$R/R_{\odot}$	No. Series
$\xi$ Per	O7.5 III(n)((f))	2450	204	14.0	2
HD 34656	O7 II(f)	2150	85	24.1	1
$\zeta$ Pup	O4 I(n)f	2250	203	19.4	2
HD 93843	O5 III(f) var	2650	100	14.0	1
68 Cyg	O7.5 III:n((f))	2550	295	15.7	3
$\lambda$ Cep	O6 I(n)fp	2250	214	21.1	3

Table 2: *IUE* Time Series

Name	Duration days	SWP range	No. of spectra	Dates yyyy/mm/dd – mm/dd	Comments
$\xi$ Per	4.4	42788 – 42918	36	1991/10/23 – 10/27	CIR
$\xi$ Per	9.4	52410 – 52652	70	1994/10/15 – 10/24	CIR
HD 34656	5.1	40728 – 40834	29	1991/01/03 – 02/06	weak N IV, $v = 0$
$\zeta$ Pup	5.3	36078 – 36168	31	1989/04/24 – 04/30	large gaps, $v = 0$
$\zeta$ Pup	15.9	53338 – 53783	149	1995/01/13 – 01/29	$v = 0$ , CIR?
HD 93843	28.1	57050 – 57329	68	1996/05/05 – 06/02	poor sampling, not used
68 Cyg	6.6	28969 – 29084	33	1986/08/23 – 08/29	large gaps, CIR?
68 Cyg	4.5	42787 – 42920	40	1991/10/22 – 10/27	weak N IV, CIR?
68 Cyg	8.6	52420 – 52650	66	1994/10/16 – 10/24	CIR
$\lambda$ Cep	5.1	40727 – 40833	24	1991/01/31 – 02/05	large gaps, $v = 0$
$\lambda$ Cep	4.5	42786 – 42919	40	1991/10/22 – 10/27	$v = 0$ , CIR?
$\lambda$ Cep	7.9	52425 – 52635	32	1994/10/16 – 10/24	poor sampling, not used

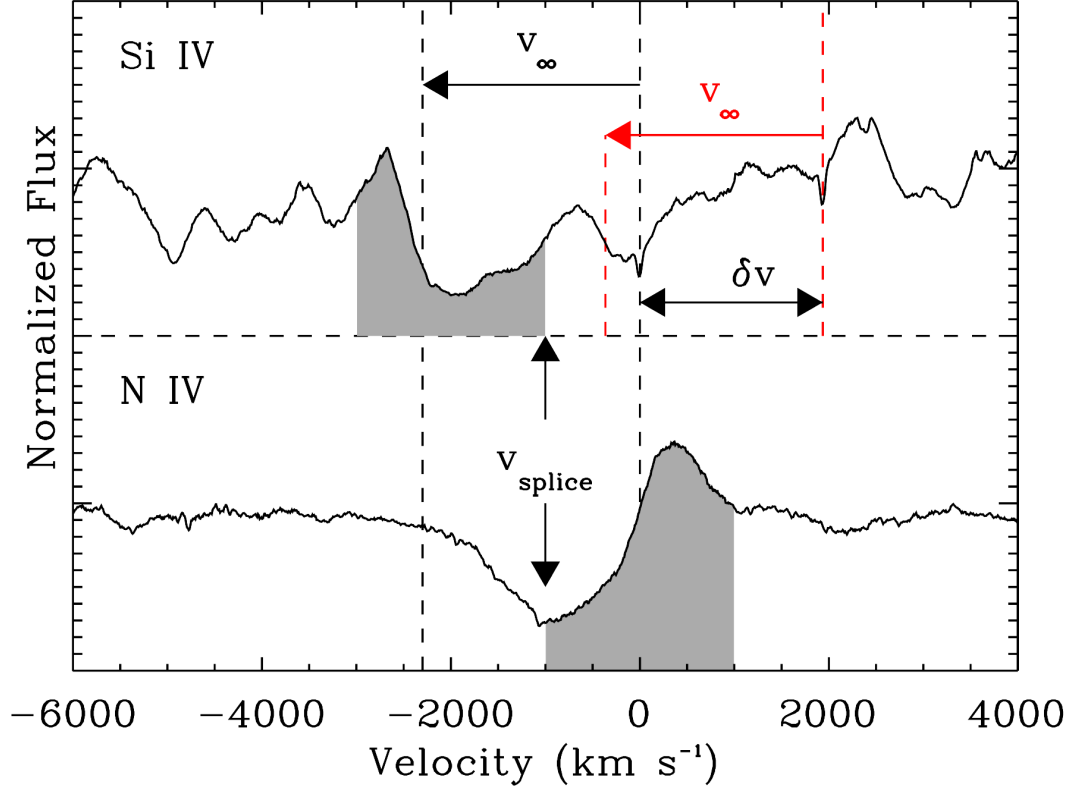


Fig. 1.— Cartoon depicting the velocity ranges used to splice together the combined Si IV and N IV dynamic spectrum. The figure shows the mean spectrum from one of the  $\zeta$  Pup time series for the Si IV region (top) as a function of velocity relative to the blue component of the doublet and the N IV region (bottom) as a function of velocity relative to its rest wavelength. Arrows indicate the ranges of the doublet profile affected by the wind, and the doublet separation. The vertical arrow indicates the velocity at which the two profiles are “stitched” together.

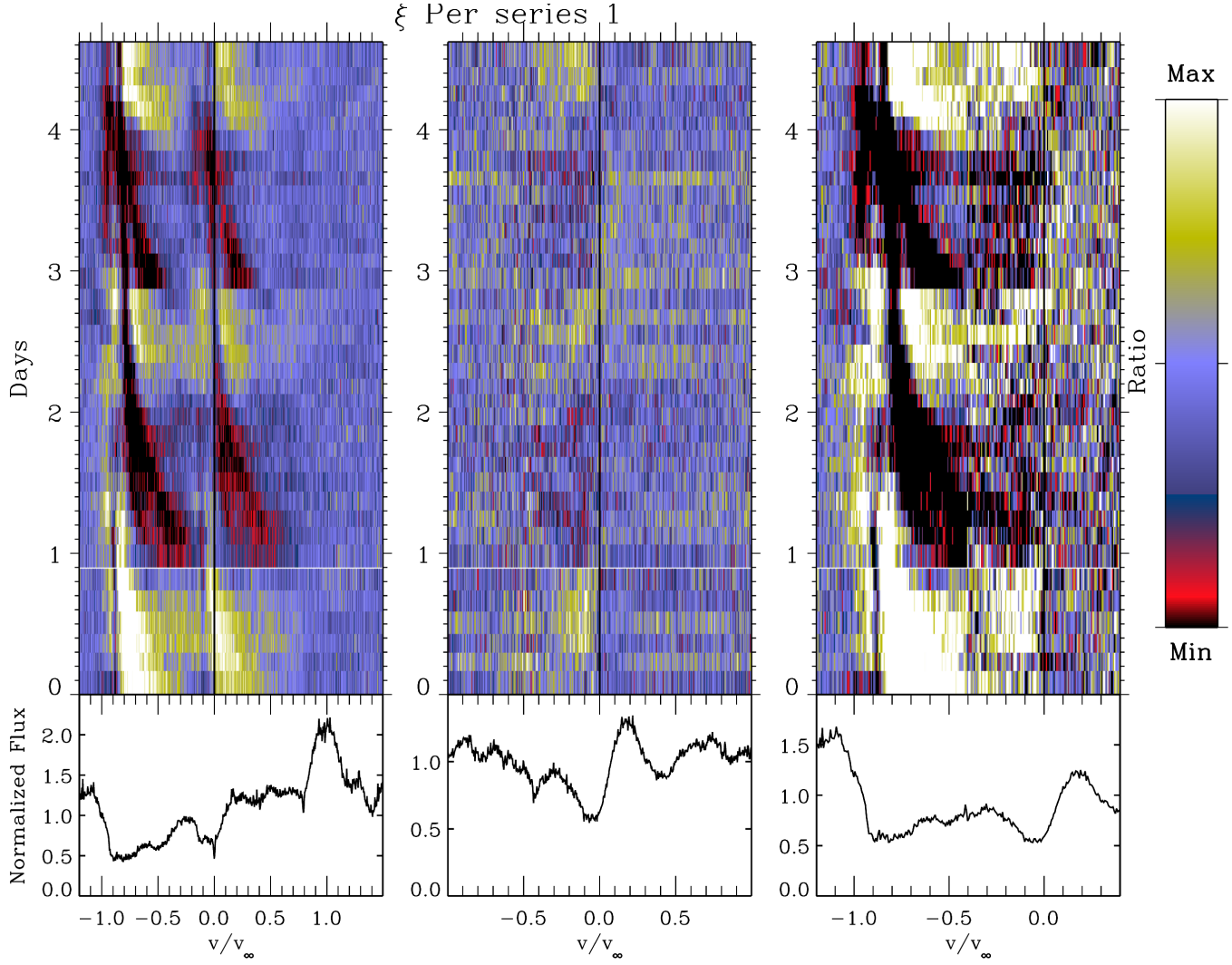


Fig. 2.— Dynamic spectra for Si IV (left), N IV (center) and the spliced spectrum (right). Each is plotted against  $w = v/v_\infty$ , where the  $v_\infty$  are from Table 1. The dynamic spectrum on the left is for Si IV  $\lambda\lambda 1400$  relative to the rest velocity of the red component,  $1402.77\text{\AA}$ , and with limits of  $1/1.4$  and  $1.4$ . The center dynamic spectrum is for N IV  $\lambda 1718$  with limits of  $1/1.2$  to  $1.2$ . The right is for the spliced line and also has limits of  $1/1.2$  to  $1.2$ . Normalized versions of the mean spectra used to normalize the images are shown below each one.

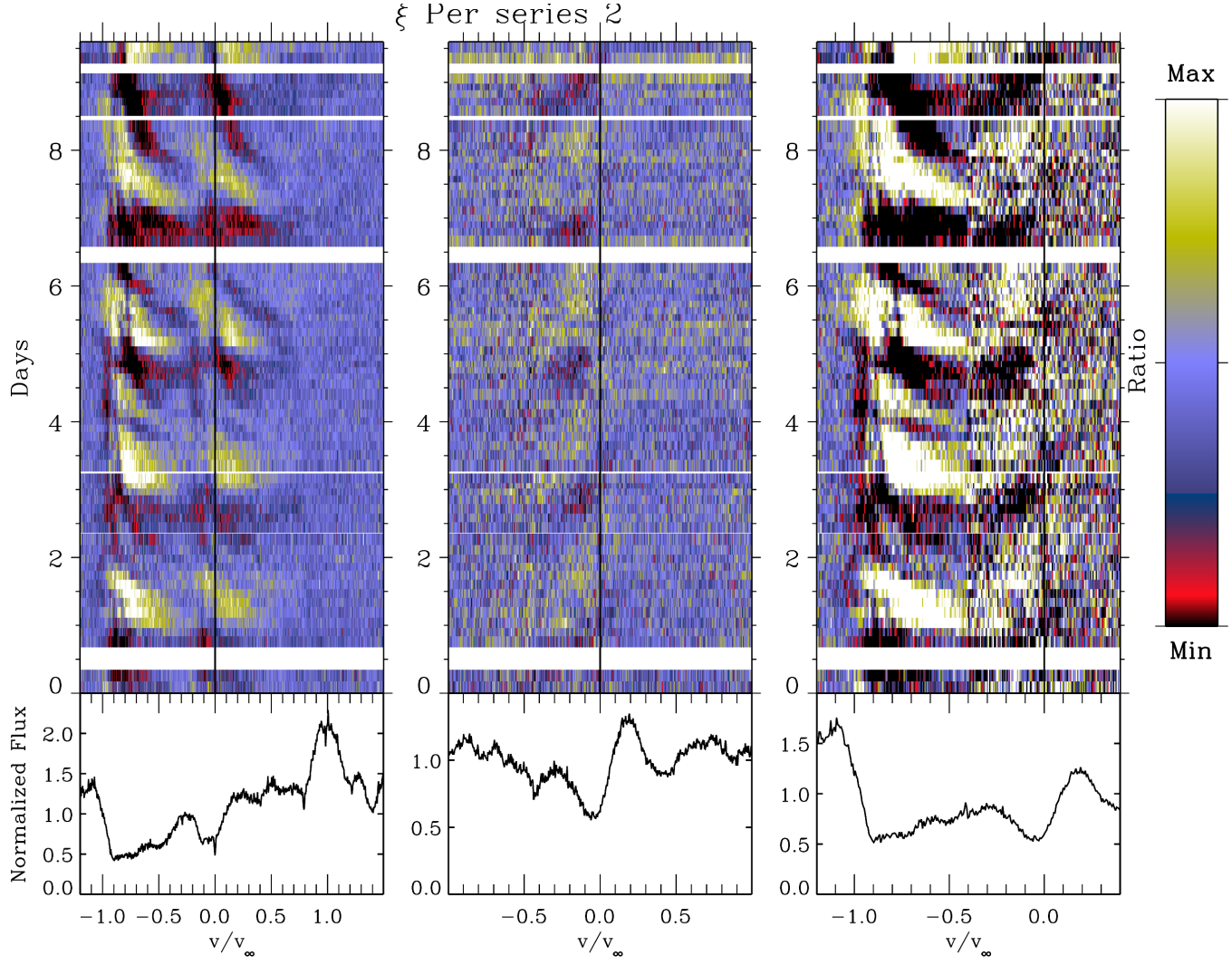


Fig. 3.— Same at Figure 2 for the second  $\xi$  Per time series.

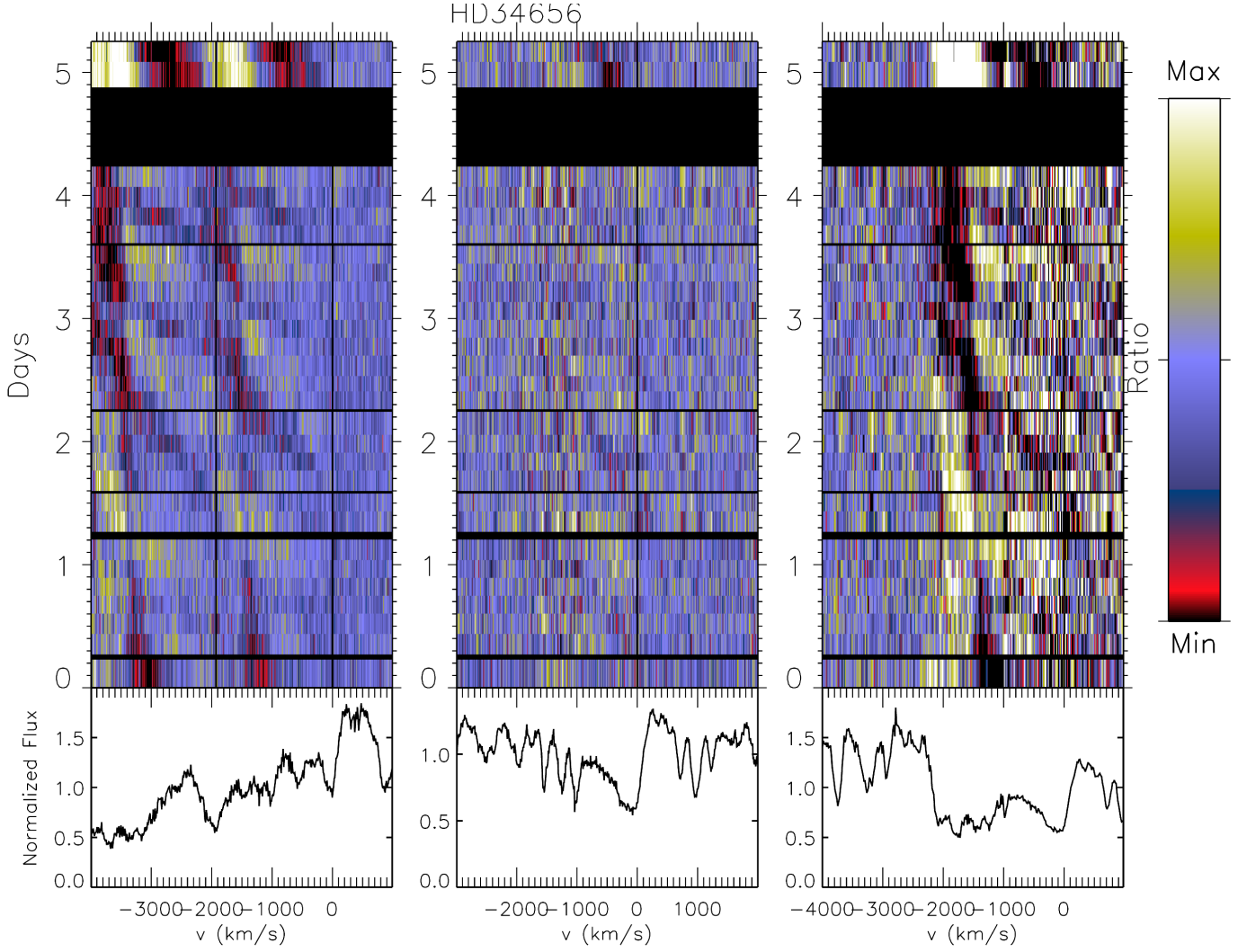


Fig. 4.— Same at Figure 2 for the HD 34656 time series.



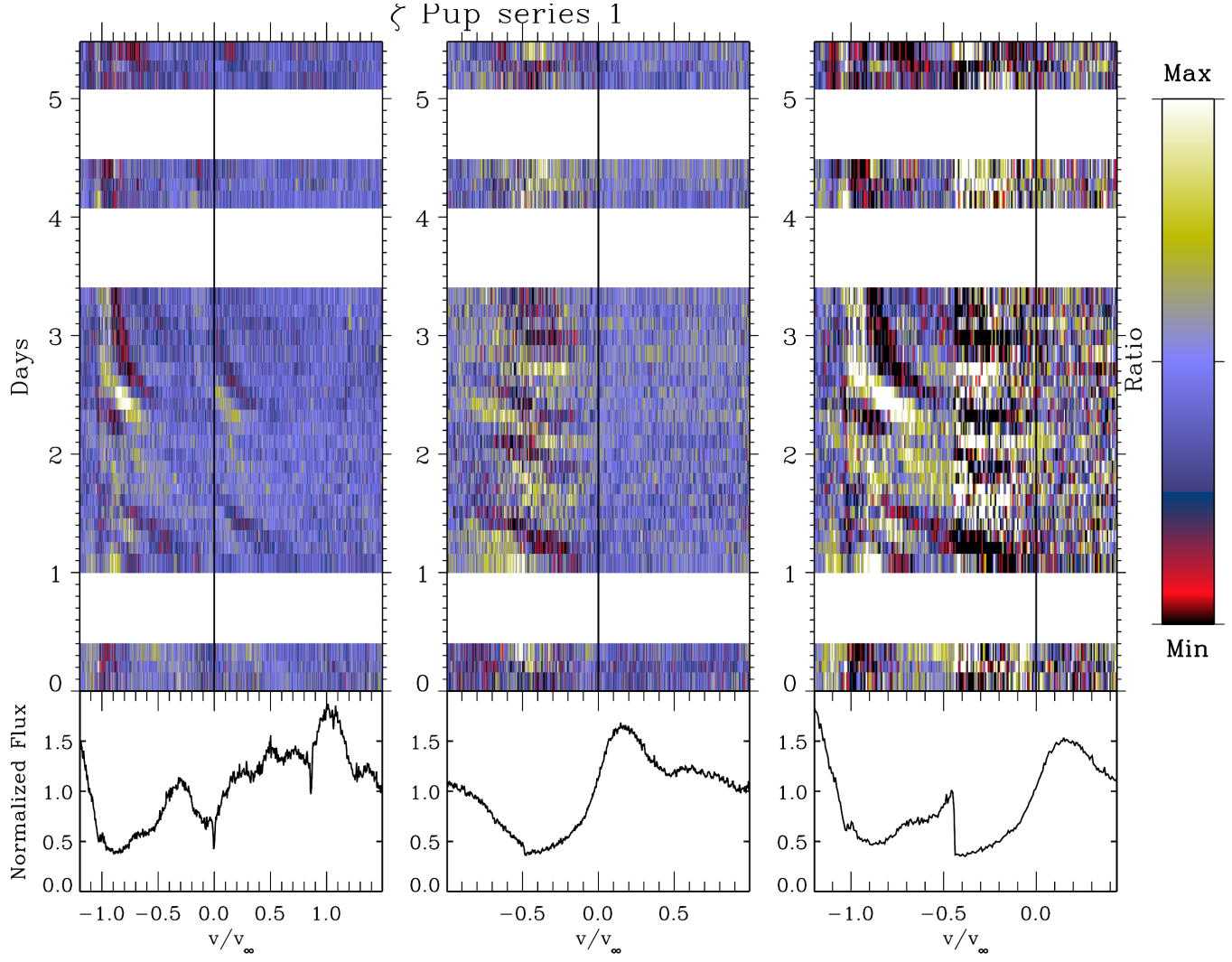


Fig. 5.— Same at Figure 2 for the first  $\zeta$  Pup time series.

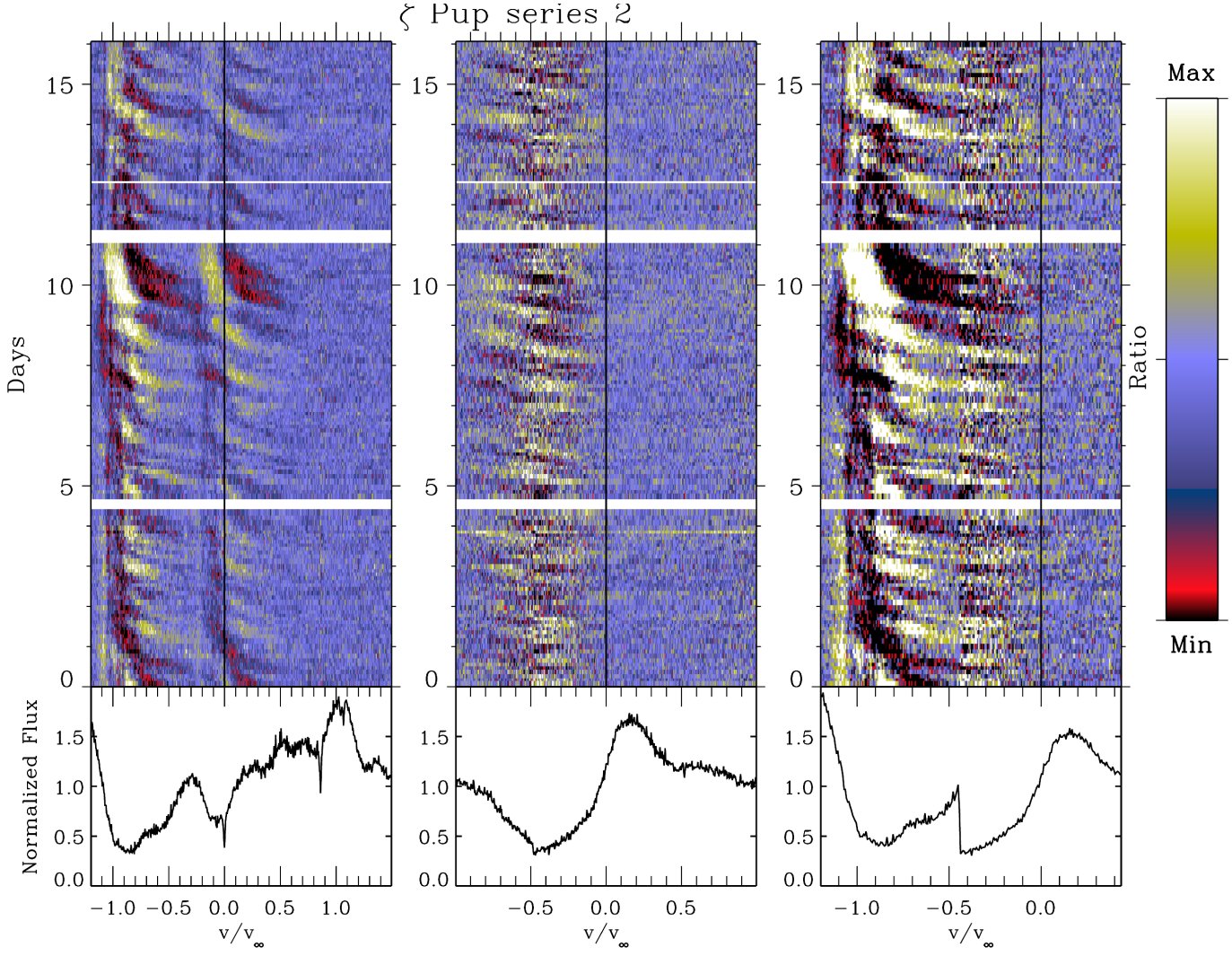


Fig. 6.— Same at Figure 2 for the first  $\zeta$  Pup time series.

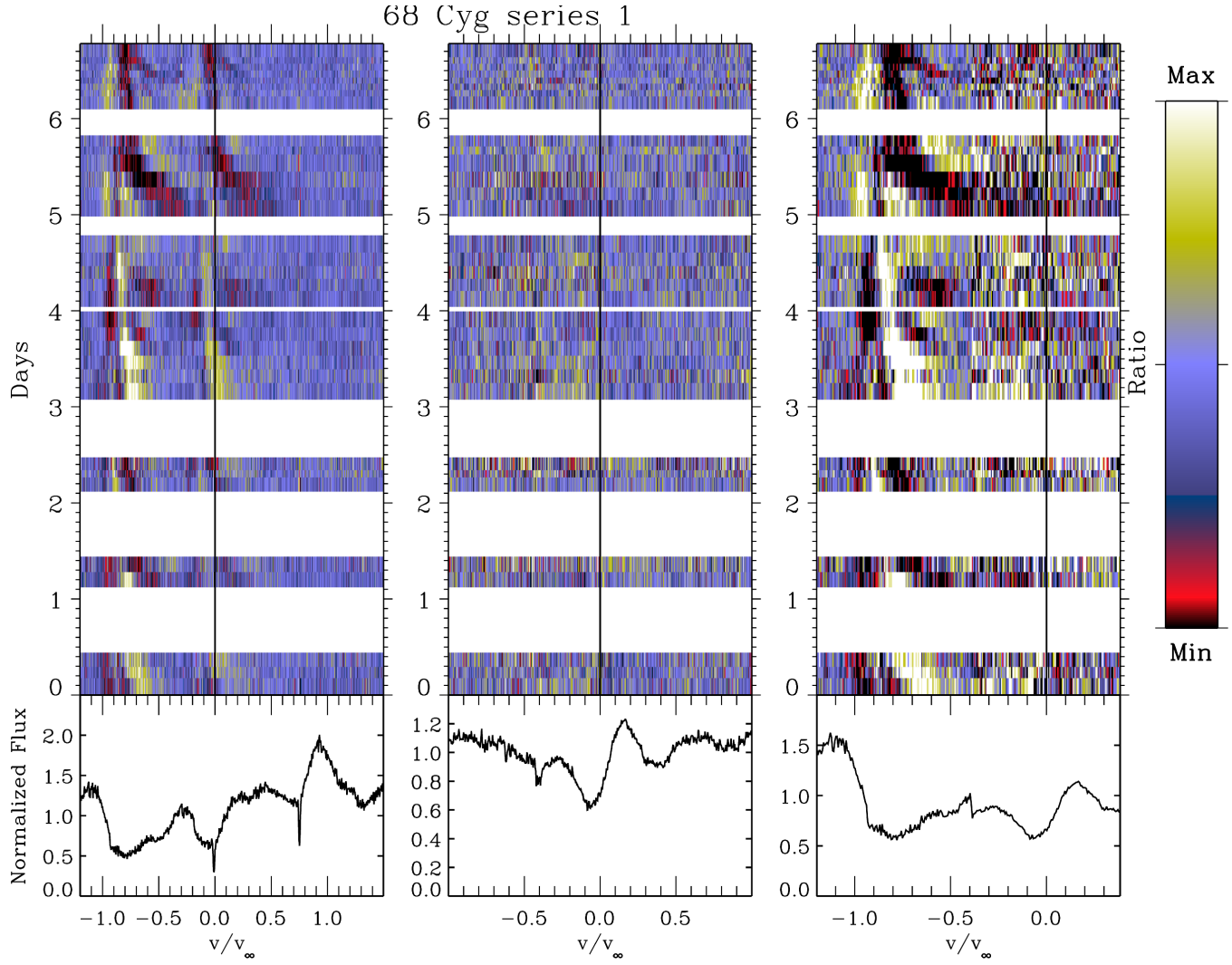


Fig. 7.— Same at Figure 2 for the first 68 Cyg time series.

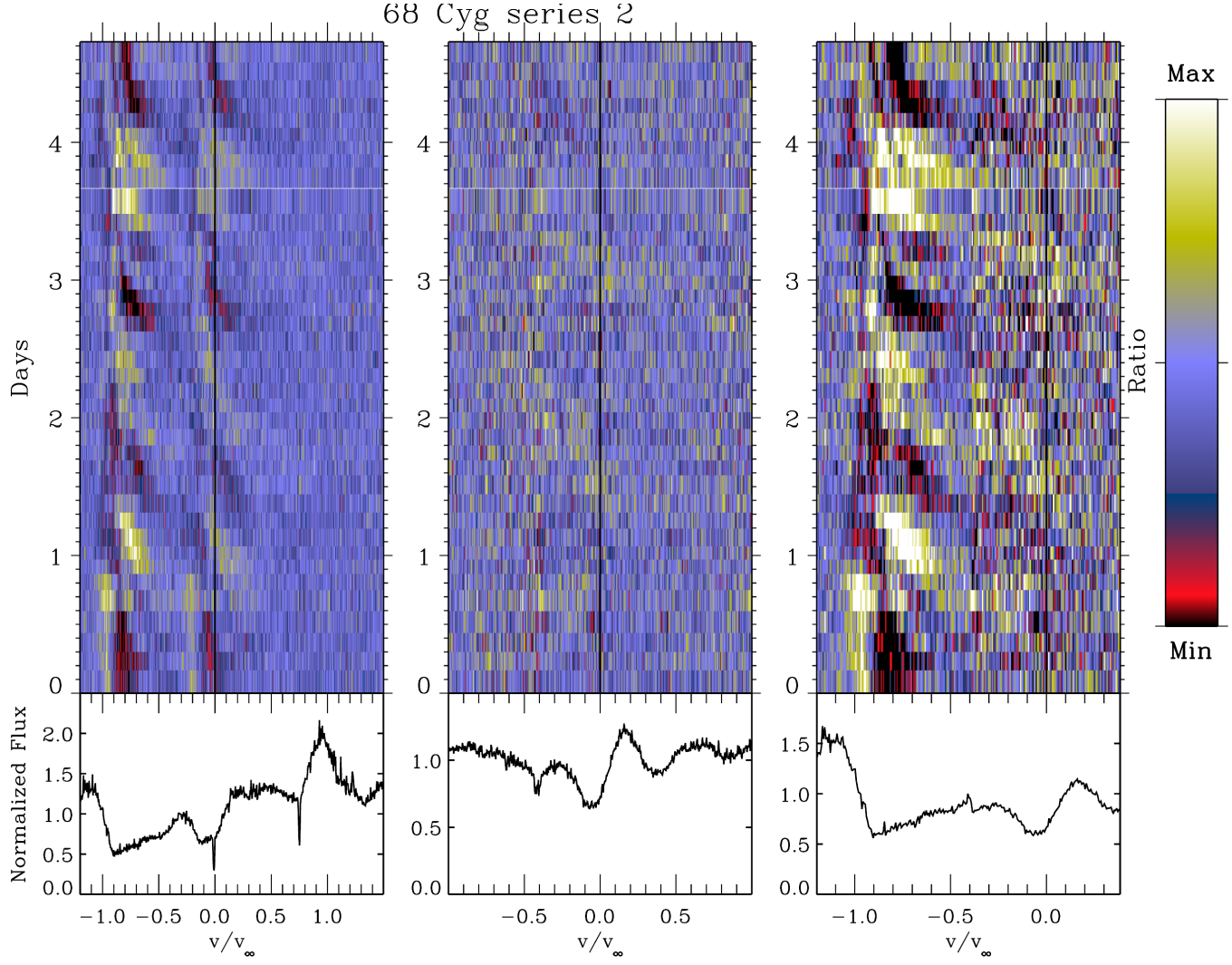


Fig. 8.— Same at Figure 2 for the second 68 Cyg time series.

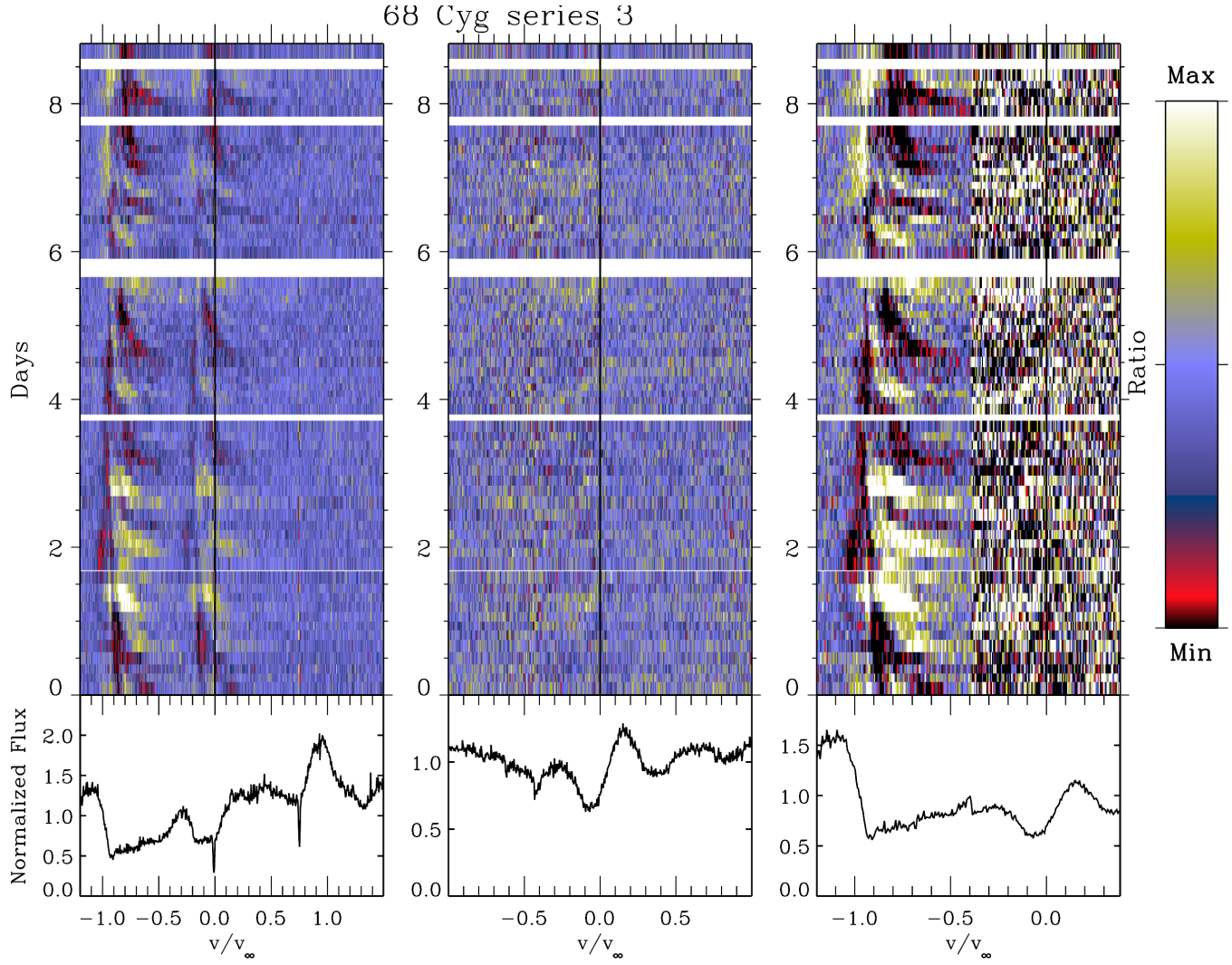


Fig. 9.— Same at Figure 2 for the first 68 Cyg time series.

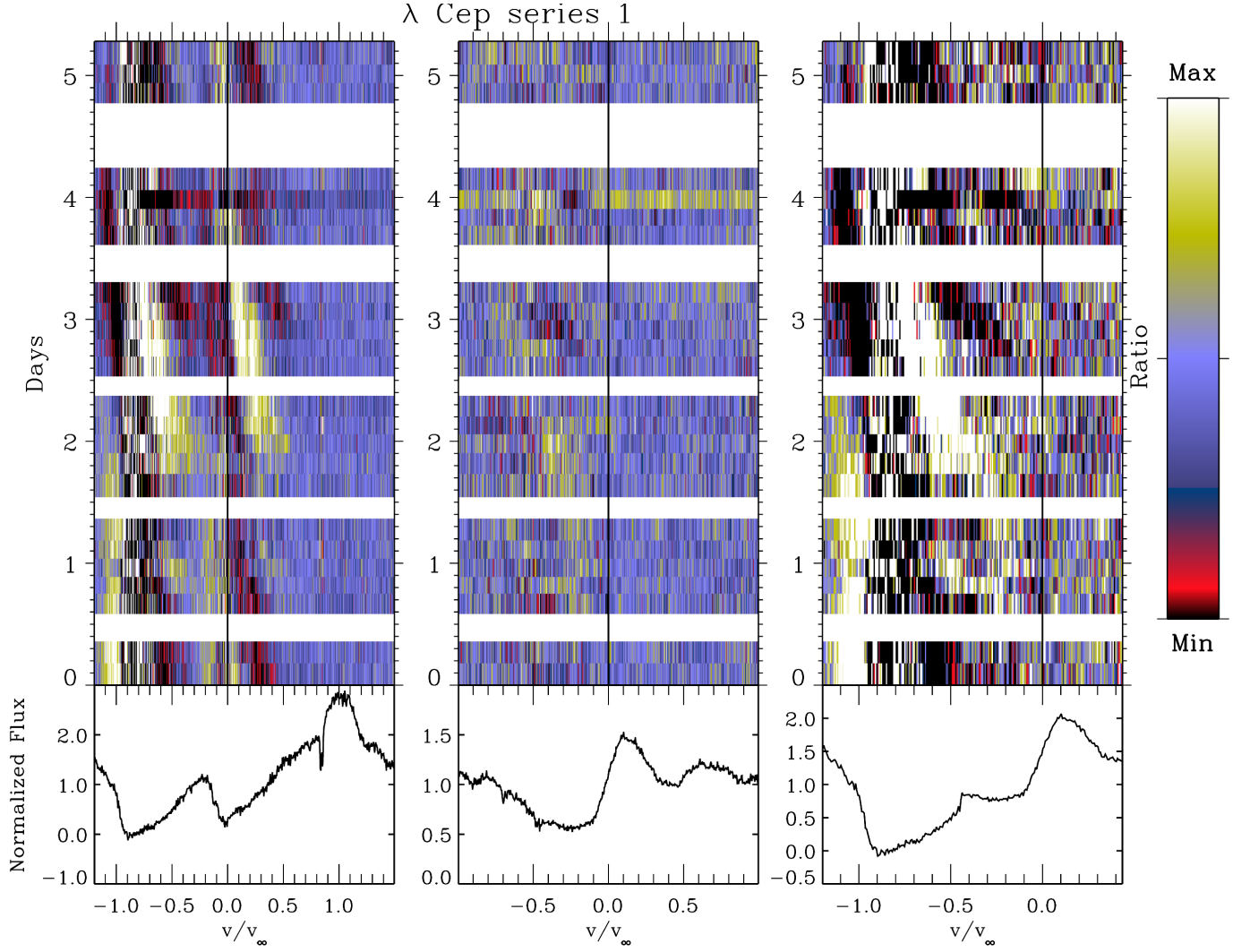


Fig. 10.— Same at Figure 2 for the first  $\lambda$  Cep time series.

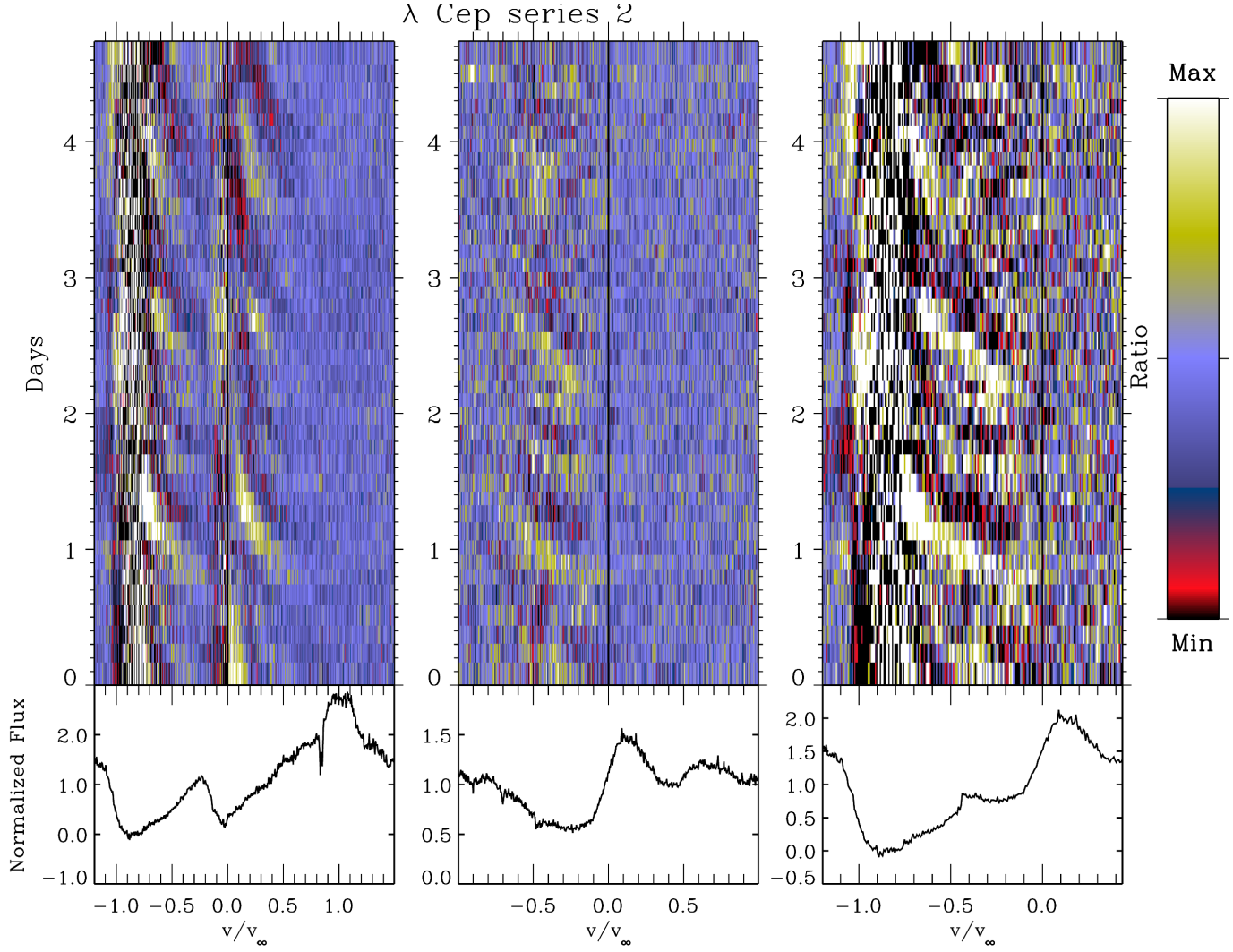


Fig. 11.— Same at Figure 2 for the second  $\lambda$  Cep time series.